ARTICLE

Theoretical Analysis of the Galloping Energy Harvesters under Bounded Random Parameter Excitation

Hang Deng, Jimin Ye[*], Wei Li[*] and Dongmei Huang

School of Mathematics and Statistics, Xidian University, Xi'an, 710071, China

*Corresponding Authors: Jimin Ye. Email: jmye@mail.xidian.edu.cn; Wei Li. Email: liweilw@mail.xidian.edu.cn

ABSTRACT

In this paper, the response properties of galloping energy harvesters under bounded random parameter excitation are studied theoretically. The first-order approximate solution of the galloping energy harvester is derived by applying the multi-scales method. The expression for the largest Lyapunov exponent that determines the trivial solution is derived, and the corresponding simulation diagrams, including the largest Lyapunov exponent diagrams and time domain diagrams, verify our results. Then the steady-state response moments of the nontrivial solution are studied using the moment method, and the analytical expressions for the first-order and second-order moments of the voltage amplitude are obtained, respectively. The corresponding results show that wind speed enhances the steady-state response moments of the voltage amplitude. Meanwhile, the voltage output can be controlled by adjusting the cubic coefficient. To further verify the response characteristics of the galloping energy harvester, the stationary probability density functions of the displacement and velocity are obtained by the Monte-Carlo simulation method. The results show that the wind speed enhances the displacement of the bluff and the damping ratios should be reduced as much as possible to improve the performance. What's more, the piezoelectric materials also impact the performance of the energy harvester.

KEYWORDS

Galloping energy harvester; multi-scales method; parametric excitation; stability

1 Introduction

In recent years, the emergence of the Internet of Things and the development of communication technology have promoted the employment of wireless sensors in various fields, such as medical and health care [1], environmental monitoring [2], industrial automation [3], etc. However, the expensive cost of replacing batteries often limits the availability of these devices. So, providing a sustainable power source for these devices is the main problem being faced. Vibration energy harvesters have been extensively studied for their potential to provide a permanent power source for the operation of these devices [4–11]. In particular, galloping energy harvesting technology has become a hot research topic in the field of flow-induced vibration energy harvesting due to the advantages of gathering high energy density during energy harvesting applications [12–17].

Generally speaking, there are five main types of flow-induced vibration energy harvesters: galloping energy harvesters [18], vortex-induced vibration (VIV) energy harvesters [19], wake-galloping energy harvesters [20], flutter energy harvesters [21] and hybrid energy harvesters based on VIV-galloping [22]. These devices can transform a part of the kinetic energy of flowing energy (e.g., wind energy, water energy) into mechanical energy, which is then into electrical power (but not limited to electrical energy) through piezoelectric materials. Among them, galloping energy harvesters with good performance in harvesting wind energy, simply designing and manufacturing, and operating in different sizes and scales, have attracted the attention and research of many scholars.

The galloping phenomenon is usually a self-excited nonlinear vibration with a high potential for high-level power output. However, due to the unstable source of wind energy, the output power of the galloping energy harvesters is sensitive to various factors. Kitio Kwuimy et al. [23] analyzed the output voltage of a galloping energy harvester under different airflow excitations and found that energy harvesting was most effective in the vicinity of the random resonance region for overcoming the potential barrier. Daqaq [24] investigated the effect of the probability density of wind direction and wind speed on the average output power of a galloping energy harvester, which given a theoretical reference for the application of small galloping energy harvesters. Xu et al. [25] obtained the optimal parameters and the critical wind speed affecting the mean square voltage of the galloping energy harvester in the fluctuating wind cases by the stochastic averaging method. Yang et al. [26] explored various factors of the average output power on a buoy platform through theoretical analysis and wind tunnel experiments, including the random excitation intensity, aerodynamic mass ratio, intrinsic frequency, and normalized electrical term. The results provide a guide toward the design of the galloping energy harvester for various requirements.

The galloping energy harvester output power is not only affected by environmental factors, but the design of the energy harvester also affects the output power. Abdelkefi et al. [27] compared the performance of galloping energy harvesters with square section and triangular section, respectively, and obtained the range of load resistance for the system to produce supercritical and subcritical instability. Yang et al. [28] compared the effects of different shapes of the bluff body with cross-section on the galloping energy harvesting efficiency, including square, rectangular, triangular, and D-shape. The results indicated that small wind energy harvesters should apply bluff bodies with square cross sections. Bibo et al. [29] found that nonlinear restoring force can enhance the output power of the galloping energy harvester. To further promote the performance of the energy harvester, Na et al. [30] changed the stiffness of the cantilever from linear to nonlinear by introducing magnetic force, broadening the range of working wind speed and improving the output power. Wang et al. [31] investigated the impact of the nonlinear magnetic force by varying the position and number of magnets, and found that the tristable energy harvester operated with lower wind speed and higher voltage output. Zhao et al. [32] changed the bluff body to a funnel shape to avoid vortex reattachment, which enhanced the fluid flow and improved the energy harvesting efficiency.

Sun et al. [33] studied a two-degree-of-freedom galloping energy harvester based on magnetically coupled, and found that the internal resonance can improve the performance of the energy harvester. In addition, scholars have also studied the effects of random noise [34,35], piezoelectric materials [36,37] and other factors [38] on the performance of the galloping energy harvester.

In recent research, environmental factors, the design, and the materials impact the harvesting efficiency of the galloping energy harvester. The cost and the inability to powerful storms also severely limit the efficacy of wind tunnel experiments. So far, scholars have only studied the effect of external excitation on the galloping energy harvester. Variations in the internal parameters of

the galloping energy harvesters caused by external excitation have not been explored. Therefore, a rigorous mathematical analysis of the parametric excitation can reveal the response mechanism and provide good guidance for the design, manufacture, and optimization of the galloping energy harvester. Meanwhile, due to the vibration of the cantilever beam is always limited to a certain range, the bounded noise is used to replace the internal random factors of the galloping energy harvester.

In this paper, response characteristics of galloping energy harvester under the bounded random parametric excitation is studied theoretically. In Section 2, the theoretical model of wind energy harvester is introduced. In Section 3, the first-order approximate solution of the response displacement and output voltage of the galloping energy harvester is given, respectively. And the stability analysis is shown in Section 4. The response characteristic analysis based on the theoretical and numerical results is presented in Section 5. Some special results are obtained in the end.

2 Mathematical Model

Galloping typically occurs in flexile, lightweight structures with angular, non-streamlined cross-sections [39]. A schematic of the bluff body undergoing galloping is shown in Fig. 1. The bluff body starts to oscillate when the flow velocity U of the wind exceeds a critical value (i.e., cut-in wind speed). The oscillation of the bluff body increases the attack angle α, thus generating more aerodynamic forces F_z. In turns, the generating aerodynamic forces F_z further increase the vertical amplitude z of the bluff body, resulting in continuous self-excited vibrations until the structure that is the aerodynamic and restoring forces limits the amplitude.

z : Vertical displacement. F_z : Aerodynamic force. U : Wind speed.

$\dot{z}$: Oscillation velocity of bluff body. U_{rel} : Relative velocity between the wind and the bluff body. α : Attack angle.
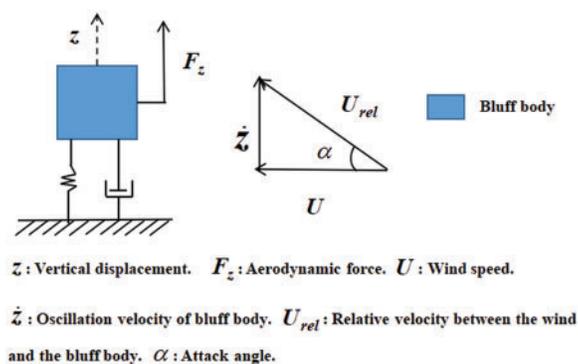
Figure 1: A schematic of the bluff body undergoing galloping

Due to the characteristics of galloping phenomenon, researchers added a pair of piezoelectric layers to the beam, using the piezoelectric effect to convert the vibration energy into electrical energy [40,41]. A schematic of the galloping energy harvester is plotted in Fig. 2, which mainly consists of load resistance, piezoelectric layers, cantilever beam, and bluff body. The bluff body makes an unstable motion in the y-direction under the wind speed U, which deforms the piezoelectric layer attached to the cantilever beam and then generates electricity and voltage across the load resistance R.
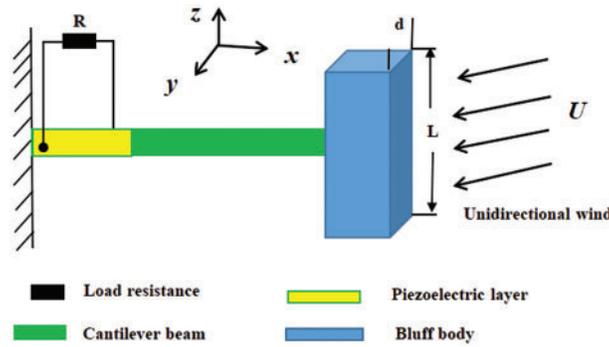
Figure 2: A schematic of the galloping energy harvester

For galloping energy harvesters, the excellent design must consider the impact of the surrounding random factors on the performance in practical applications. Herein, this paper focuses on the response characteristics of the galloping energy harvester under random parameter excitation. According to [42,43], the corresponding mathematical model of the galloping energy harvester under random parameter excitation shown in Fig. 2 can be expressed as:

$$M\ddot{Y}(t) + C\dot{Y}(t) + F_r(t) - \theta V(t) = F_y + F\xi(t)Y(t), \tag{1}$$

$$C_p\dot{V}(t) + \frac{V(t)}{R} + \theta\dot{Y}(t) = 0, \tag{2}$$

where $Y(t)$ and $V(t)$ represent the displacement of the bluff body in the y-direction and the voltage of the galloping energy harvester, respectively. M is the effective mass of bluff body and cantilever beam. C and θ are the damping coefficient and electromechanical coupling coefficient, respectively. C_p and R denote the equivalent capacitance and equivalent load resistance, respectively. F_r is the nonlinear restoring force. F_y is the aerodynamic force. $\xi(t)$ is the bounded random excitation and F is the corresponding density. The dot represents the derivative with respect to time t.

For the model to describe the oscillation characteristics of the galloping energy harvester more accurately, a nonlinear restoring force is employed in this study [29]. The nonlinear restoring force F_r is assumed as $F_r = k_1Y + k_2Y^3$, where k_1 and k_2 are the linear stiffness coefficient and the cubic stiffness coefficient, respectively. Meanwhile, the oscillation velocity of the bluff body is much smaller than the wind speed in the galloping phenomenon. Therefore, the aerodynamic force F_y is considered using the quasi-steady hypothesis that has been verified in many studies to simulate galloping effectively [25]. It can be expressed in the following polynomial for the velocity of the bluff body and the wind speed:

$$F_y = \frac{1}{2}\rho U^2 S\left[a_1\frac{\dot{Y}}{U} - a_2\left(\frac{\dot{Y}}{U}\right)^3\right], \tag{3}$$

where ρ and U are the air density and the wind speed, respectively. S represents the area on the windward facing side of the bluff body. The corresponding expression is $S = Ld$, where L and d are the height and width on the windward side of the bluff body in Fig. 2, respectively. a_1 and a_2 are the aerodynamic coefficients and aspect ratio of the bluff body, respectively.

From the application perspective, it is unavoidable that the energy harvester will be influence by the stochastic factors from the system itself. Herein, an ergodic bounded random excitation $\xi(t)$ with

zero mean is employed in the model [44,45]. It can be expressed as follows:

$$\xi(t) = \cos(\Omega t + \widetilde{\beta} W(t)), \tag{4}$$

where Ω and $\widetilde{\beta}$ are the center frequency and the bandwidth of the random excitation, respectively. $W(t)$ is the standard Wiener process.

Next, to facilitate the analysis, scaled transformed $(y, v) \rightarrow \left(\dfrac{Y}{d}, \dfrac{C_p}{\theta d}V\right)$ is employed for Eqs. (1) and (2). The obtained equations can be expressed as follows:

$$\ddot{y}(t) + b_1\dot{y}(t) + b_2\dot{y}^3(t) + \omega^2 y(t) + \gamma y^3(t) - sv(t) = f\xi(t)y(t), \tag{5}$$

$$\dot{v}(t) + \alpha v(t) + \dot{y}(t) = 0, \tag{6}$$

where $b_1 = \zeta - \mu a_1 \overline{U}$, $b_2 = \dfrac{\mu a_2}{\overline{U}}$, $\omega^2 = \dfrac{k_1}{M}$, $\gamma = \dfrac{k_2 d^2}{M}$, $s = \dfrac{\theta^2}{C_p M}$, $f = \dfrac{F}{M}$, $\alpha = \dfrac{1}{C_p R}$, $\overline{U} = \dfrac{U}{d}$, $\zeta = \dfrac{C}{M}$, and $\mu = \dfrac{\rho L d^2}{2M}$. Then, the theoretical analysis of the dimensionless model will be discussed in the next section.

3 First-Order Approximate Solutions

In this section, due to the property that the speed of the bluff body motion is much slower than the wind speed in the galloping phenomenon, the multi-scales method is used to analyze the approximate analytical solution. Firstly, assume that the approximate solutions under multiple timescales of Eqs. (5) and (6) can be expressed as follows:

$$y(t, \varepsilon) = y_0(T_0, T_1) + \varepsilon y_1(T_0, T_1) + \cdots, \tag{7}$$

$$v(t, \varepsilon) = v_0(T_0, T_1) + \varepsilon v_1(T_0, T_1) + \cdots, \tag{8}$$

where $T_n = \varepsilon^n t$ and ε are a small parameter. Meanwhile, considering that the bluff body is affected by minor perturbations, the coefficients in Eq. (6) are assumed as follows:

$$b_1 \rightarrow \varepsilon b_1, b_2 \rightarrow \varepsilon b_2, \gamma \rightarrow \varepsilon\gamma, s \rightarrow \varepsilon s, f \rightarrow \varepsilon f. \tag{9}$$

Defining the derivative operators represented by the partial derivative operators $D_0 = \dfrac{\partial}{\partial T_0}$, $D_1 = \dfrac{\partial}{\partial T_1}$ and $D_2 = \dfrac{\partial}{\partial T_2}$, the corresponding expressions can be obtained as follows:

$$\frac{d}{dt} = D_0 + \varepsilon D_1 + \varepsilon^2 D_2 + \cdots, \tag{10}$$

$$\frac{d^2}{dt^2} = D_0^2 + 2\varepsilon D_0 D_1 + \varepsilon^2 \left(D_1^2 + 2D_0 D_2\right) + \cdots, \tag{11}$$

Substituting Eqs. (7)–(11) into Eqs. (6) and (7), then the coefficients of the same power of ε^0 and ε^1, respectively, can be obtained as follows:

ε^0 :

$$D_0^2 y_0(T_0, T_1) + \omega^2 y_0(T_0, T_1) = 0, \tag{12}$$

$$D_0^2 v_0(T_0, T_1) + \alpha v_0(T_0, T_1) = -D_0 y_0(T_0, T_1). \tag{13}$$

ε^1 :

$$\begin{aligned} D_0^2 y_1(T_0, T_1) + \omega^2 y_1(T_0, T_1) = & -2D_0 D_1 y_0(T_0, T_1) \\ & - b_1 D_0 y_0(T_0, T_1) - b_2(D_0 y_0(T_0, T_1))^3 - \gamma y_0^3(T_0, T_1) \\ & + s v_0(T_0, T_1) + f \cos(\Omega T_0 + \beta W(T_1)) y_0(T_0, T_1), \end{aligned} \tag{14}$$

$$D_0 v_1(T_0, T_1) + \alpha v_1(T_0, T_1) = -(D_0 y_1(T_0, T_1) + D_1 y_0(T_0, T_1)) - D_1 v_0(T_0, T_1), \tag{15}$$

where $\beta = \dfrac{\widetilde{\beta}}{\sqrt{\varepsilon}}$. Then, according to Eqs. (12) and (13), the general solutions can be written as following:

$$y_0(T_0, T_1) = A(T_1) \cos(\omega T_0 + \varphi(T_1)), \tag{16}$$

$$v_0(T_0, T_1) = \frac{\omega A(T_1)}{\alpha^2 + \omega^2} (\alpha \sin(\omega T_0 + \varphi(T_1)) - \omega \cos(\omega T_0 + \varphi(T_1)), \tag{17}$$

where $A(T_1)$ and $\varphi(T_1)$ denote the amplitude and phase, respectively, and are both the functions of the time scale T_1. Then, substituting Eqs. (16) and (17) into Eq. (14), the corresponding equation can be obtained as follows:

$$\begin{aligned} D_0^2 y_1(T_0, T_1) + \omega^2 y_1(T_0, T_1) = & \; 2\omega A'(T_1) \sin(\omega T_0 + \varphi(T_1)) + 2\omega \varphi' A(T_1) \cos(\omega T_0 + \varphi(T_1)) \\ & + b_1 \omega A(T_1) \sin(\omega T_0 + \varphi(T_1)) + b_2 \omega^3 A^3(T_1) \sin^3(\omega T_0 + \varphi(T_1)) \\ & - \gamma A^3(T_1) \cos^3(\omega T_0 + \varphi(T_1)) + \frac{s\omega A(T_1)}{\alpha^2 + \omega^2} \cdot \\ & (\alpha \sin(\omega T_0 + \varphi(T_1)) - \omega \cos(\omega T_0 + \varphi(T_1)) \\ & + \frac{fA(T_1)}{2} \cos((\Omega + \omega) T_0 + \beta W(T_1) + \varphi(T_1)) \\ & + \frac{fA(T_1)}{2} \cos((\Omega - \omega) T_0 + \beta W(T_1) - \varphi(T_1)), \end{aligned} \tag{18}$$

It can be observed that Eq. (18) will produce resonance terms when the excitation frequency $\Omega \approx 2\omega$. For this, a tuning parameter σ is introduced to study the main resonance response of the energy harvester. The excitation frequency Ω is denoted as $\Omega = 2\omega + \varepsilon\sigma$ and a new variable $\eta(T_1) = \sigma T_1 + \beta W(T_1) - 2\varphi(T_1)$ is employed. Then, substituting Ω and $\eta(T_1)$ into Eq. (18) and eliminating the resonance terms, the following equations can be driven:

$$A'(T_1) = -\frac{b_1}{2} A(T_1) - \frac{3b_2 \omega^2 A^3(T_1)}{8} - \frac{s\alpha A(T_1)}{2(\alpha^2 + \omega^2)} + \frac{fA(T_1)}{4\omega} \sin \eta, \tag{19}$$

$$A\left(T_1\right)\eta'\left(T_1\right) = \sigma A\left(T_1\right) - \frac{3\gamma A^3(T_1)}{4\omega} - \frac{s\omega A(T_1)}{\alpha^2 + \omega^2} + \frac{fA(T_1)}{2\omega}\cos\eta + \beta A\left(T_1\right)W'\left(T_1\right). \tag{20}$$

After solving A and η, the first-order uniform expansions of the response displacement and the output voltage, respectively, are given as following:

$$y = A\left(\varepsilon t\right)\cos\left(\frac{\Omega}{2}t - \frac{\eta(\varepsilon t)}{2}\right) + O\left(\varepsilon\right), \tag{21}$$

$$v = \frac{\omega A(\varepsilon t)}{\alpha^2 + \omega^2}\left(\alpha\sin\left(\frac{\Omega}{2}t - \frac{\eta(\varepsilon t)}{2}\right) - \omega\cos\left(\frac{\Omega}{2}t - \frac{\eta(\varepsilon t)}{2}\right)\right) + O\left(\varepsilon\right)$$

$$= \frac{\omega}{\sqrt{\alpha^2 + \omega^2}}A\left(\varepsilon t\right)\sin\left(\frac{\Omega}{2}t - \frac{\eta(\varepsilon t)}{2} - art\tan\frac{\omega}{\alpha}\right) + O\left(\varepsilon\right). \tag{22}$$

4 Stability and Moment Analysis

In this section, the stability of the trivial solutions and nontrivial solutions are discussed, respectively. Evidently, $A = 0$ is the trivial solution of the Eqs. (19) and (20). Herein, the stability will be analyzed firstly. The corresponding linearized equations can be written as follows:

$$A'\left(T_1\right) = -\frac{b_1}{2}A\left(T_1\right) - \frac{s\alpha A(T_1)}{2(\alpha^2 + \omega^2)} + \frac{fA(T_1)}{4\omega}\sin\eta, \tag{23}$$

$$A\left(T_1\right)\eta'\left(T_1\right) = \sigma A\left(T_1\right) - \frac{s\omega A(T_1)}{\alpha^2 + \omega^2} + \frac{fA(T_1)}{2\omega}\cos\eta + \beta A\left(T_1\right)W'\left(T_1\right). \tag{24}$$

Let $\rho = \ln A$, and the Eqs. (23) and (24) can be expressed in the form of It^o stochastic differential equations as follows:

$$d\rho = \left(-\frac{b_1}{2} - \frac{s\alpha}{2(\alpha^2 + \omega^2)} + \frac{f}{4\omega}\sin\eta\right)dT_1, \tag{25}$$

$$d\eta = \left(\sigma - \frac{s\omega}{\alpha^2 + \omega^2} + \frac{f}{2\omega}\cos\eta\right)dT_1 + \beta dW. \tag{26}$$

It is apparent from Eqs. (25) and (26) that $\eta(T_1)$ is an ergodic random process and the corresponding stationary probability density function (PDF) $p(\eta)$ can be derived based on the Fokker-Planck-Kolmogorov (FPK) equation as follows:

$$\frac{d^2p}{d\eta^2} - \frac{d}{d\eta}\left[\left(\overline{\sigma} - \overline{f}\cos\eta\right)p\right] = 0, \tag{27}$$

where $\overline{\sigma} = 2\left(\dfrac{\sigma}{\beta^2} - \dfrac{s\omega}{\beta^2(\alpha^2 + \omega^2)}\right)$ and $\overline{f} = -\dfrac{f}{\omega\beta^2}$. Since $p(\eta)$ satisfies both the normality condition (i.e., $\int_0^{2\pi}p(\eta)d\eta = 1$) and the periodicity condition (i.e., $p(\eta) = p(\eta + 2\pi)$), it can be derived from

Eq. (27) as follows:

$$p(\eta) = \frac{\exp\left(\overline{\sigma}(\eta + \pi) + \overline{f}\sin\eta\right)}{4\pi^2 I_{i\sigma}\left(\overline{f}\right) I_{-i\sigma}\left(\overline{f}\right)} \int_{\eta}^{\eta + 2\pi} \exp\left(-\overline{\sigma}x + \overline{f}\sin x\right) dx, \tag{28}$$

where $I_{i\sigma}\left(\overline{f}\right)$ and $I_{-i\sigma}\left(\overline{f}\right)$ are the first kind of modified Bessel functions.

Next the Lyapunov exponent is employed to study the stability of the trivial solutions. For any initial values (A_0, η_0) of Eqs. (23) and (24), the corresponding Lyapunov exponent of any solutions $A(T_1, A_0, \eta_0)$ can be expressed as follows:

$$\lambda(A_0, \eta_0) = \lim_{T_1 \to \infty} \frac{1}{T_1} \ln[A(T_1, A_0, \eta_0)], w.p.1, \tag{29}$$

where $w.p.1$ is with probability one. Meanwhile, the stability depends on the largest Lyapunov exponent, which can be derived as follows:

$$\lambda(A_0, \eta_0) = \lim_{T_1 \to \infty} \frac{1}{T_1} \ln\left[\frac{A(T_1)}{A(0)}\right] = \lim_{T_1 \to \infty} \frac{1}{T_1}(\rho(T_1) - \rho(0))$$

$$= -\frac{b_1}{2} - \frac{s\alpha}{2(\alpha^2 + \omega^2)} + \lim_{T_1 \to \infty} \frac{1}{T_1} \int_0^{T_1} \frac{f}{4\omega} \sin(\tau) d\tau$$

$$= -\frac{b_1}{2} - \frac{s\alpha}{2(\alpha^2 + \omega^2)} + \frac{f}{8\omega}\left(\frac{I_{1-i\sigma}\left(-\overline{f}\right)}{I_{-i\sigma}\left(-\overline{f}\right)} + \frac{I_{1+i\sigma}\left(-\overline{f}\right)}{I_{i\sigma}\left(-\overline{f}\right)}\right). \tag{30}$$

The trivial solution of Eqs. (23) and (24) is stable when $\lambda < 0$, and unstable when $\lambda > 0$, which mainly depends on the above parameters.

Next, the moment method will be used to study the stability of nontrivial solutions. And the Itˆo stochastic differential equations can be derived as follows:

$$dA = \left(-\frac{b_1}{2}A - \frac{3b_2\omega^2 A^3}{8} - \frac{s\alpha A}{2(\alpha^2 + \omega^2)} + \frac{fA}{4\omega}\sin\eta\right) dT_1, \tag{31}$$

$$d\eta = \left(\sigma A - \frac{3\gamma A^2}{4\omega} - \frac{s\omega}{\alpha^2 + \omega^2} + \frac{f}{2\omega}\cos\eta\right) dT_1 + +\beta dW. \tag{32}$$

For the deterministic case of $\beta = 0$, the nontrivial solutions A^* and η^* of Eqs. (19) and (20), which can be obtained from $A' = 0$ and $\eta' = 0$, are governed by the following equations:

$$-\frac{b_1}{2} - \frac{3b_2\omega^2 A^{*2}}{8} - \frac{s\alpha}{2(\alpha^2 + \omega^2)} + \frac{f}{4\omega}\sin\eta^* = 0, \tag{33}$$

$$\sigma - \frac{3\gamma A^{*2}}{4\omega} - \frac{s\omega}{\alpha^2 + \omega^2} + \frac{f}{2\omega}\cos\eta^* = 0. \tag{34}$$

To explore the impact of random excitation, the perturbation terms $\widetilde{A}$ and $\widetilde{\eta}$ are introduce. Then the nontrivial solution of Eqs. (19) and (20) can be expressed as follows:

$$A = A^* + \widetilde{A}, \tag{35}$$

$$\eta = \eta^* + \widetilde{\eta}. \tag{36}$$

Substituting Eqs. (35) and (36) into Eqs. (31) and (32), the linearized differential equations with respect to the perturbation terms $\widetilde{A}$ and $\widetilde{\eta}$ can be obtained as follows:

$$d\widetilde{A} = \left(-\frac{3b_2\omega^2 A^{*2}}{4}\widetilde{A} + \frac{fA^*}{4\omega}\cos\eta^*\widetilde{\eta}\right)dT_1, \tag{37}$$

$$d\widetilde{\eta} = -\left(\frac{3\gamma A^*}{2\omega}\widetilde{A} + \frac{f}{2\omega}\sin\eta^*\widetilde{\eta}\right)dT_1 + +\beta dW. \tag{38}$$

According to Eqs. (37) and (38), combining the moment method and the property as follows:

$$\frac{dE\widetilde{A}}{dT_1} = \frac{dE\widetilde{\eta}}{dT_1} = \frac{dE\widetilde{A}^2}{dT_1} = \frac{dE\widetilde{A}\widetilde{\eta}}{dT_1} = \frac{dE\widetilde{\eta}^2}{dT_1} = 0, \tag{39}$$

the perturbation terms $\widetilde{A}$ and $\widetilde{\eta}$ can be derived as follows for the first-order and second-order steady-state moments:

$$E\widetilde{A} = E\widetilde{\eta} = 0, \tag{40}$$

$$E\widetilde{A}^2 = \frac{\omega f \cos^2\eta^*\beta^2}{3\left(3A^{*2}\sin\eta^* b_2^2\omega^6 + 3A^{*2}\cos\eta^* b_2\omega^3\gamma + 2\sin^2\eta^* b_2 f\omega^3 + \sin(2\eta^*)\gamma f\right)}, \tag{41}$$

$$E\widetilde{A}\widetilde{\eta} = \frac{b_2\beta^2\omega^4 A^*\cos\eta^*}{3A^{*2}\sin\eta^* b_2^2\omega^6 + 3A^{*2}\cos\eta^* b_2\omega^3\gamma + 2\sin^2\eta^* b_2 f\omega^3 + \sin(2\eta^*)\gamma f}, \tag{42}$$

$$E\widetilde{\eta}^2 = \frac{\omega\beta^2(3A^{*2}b_2^2\omega^6 + 2fb_2\omega^3\sin\eta^* + 2\gamma f\cos\eta^*)}{f\left(3A^{*2}\sin\eta^* b_2^2\omega^6 + 3A^{*2}\cos\eta^* b_2\omega^3\gamma + 2\sin^2\eta^* b_2 f\omega^3 + \sin(2\eta^*)\gamma f\right)}. \tag{43}$$

Therefore, the response moments of the nontrivial solutions of Eqs. (35) and (36) can be obtained from Eqs. (40) and (41) as follows:

$$EA = E\left(A^* + \widetilde{A}\right) = A^*, \tag{44}$$

$$EA^2 = A^{*2} + \frac{\omega f \cos^2\eta^*\beta^2}{3\left(3A^{*2}\sin\eta^* b_2^2\omega^6 + 3A^{*2}\cos\eta^* b_2\omega^3\gamma + 2\sin^2\eta^* b_2 f\omega^3 + \sin(2\eta^*)\gamma f\right)}. \tag{45}$$

Next, from the Eqs. (22), (44) and (45), the corresponding response moments of the voltage amplitude can be obtained as follows:

$$Ev = \frac{\omega}{\sqrt{\alpha^2 + \omega^2}}A^*, \tag{46}$$

$$Ev^2 = \frac{\omega^2}{\alpha^2 + \omega^2} EA^2. \tag{47}$$

5 Response Characteristics

In this section, the response characteristics of the galloping energy harvester are analyzed based on above theoretical results. The parameters are chosen as $M = 0.05, C = 0.025, C_p = 1 \times 10^{-9}, R = 1 \times 10^9, \theta = 1, L = 0.1, d = 0.4, k_1 = 0.05, k_2 = 0.625, \rho = 1, a_1 = 2.5, a_2 = 12.8$ unless other cases are stated.

For the case of $A = 0$, Figs. 3a and 3b are the mesh surface and isohypse curves of the largest Lyapunov exponents (LLE) λ which is determined by Eq. (30), respectively. The solutions of the LLE is divided into two different regions by the plane where the Lyapunov exponent is zero. Near the resonance region, the LLE reaches the maximum in the center of the unstable region. And outside this region, the stability region is present. To verify the results, the time-domain results are shown in Figs. 4a and 4b, respectively. The trivial solution is unstable at point $A(\sigma = 0.575$ and $f = 1.225)$ (Fig. 4a) and stable at point $B(\sigma = 0.575$ and $f = 0.625)$ (Fig. 4b).
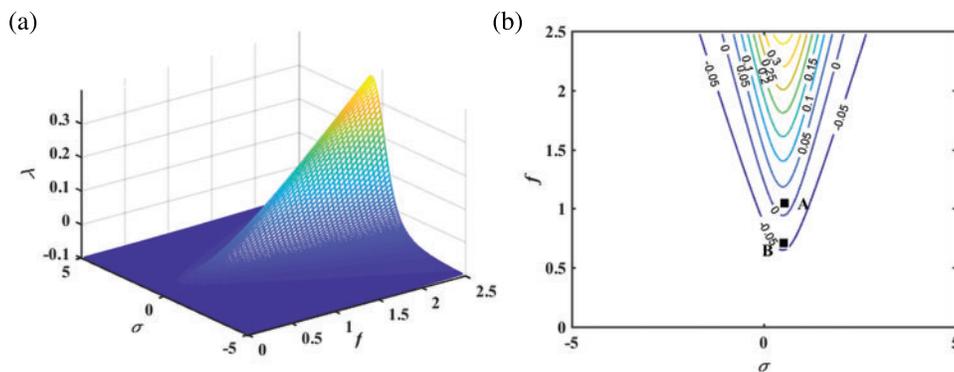
Figure 3: Largest Lyapunov exponents: (a) Mesh surface; (b) Isohypse curves
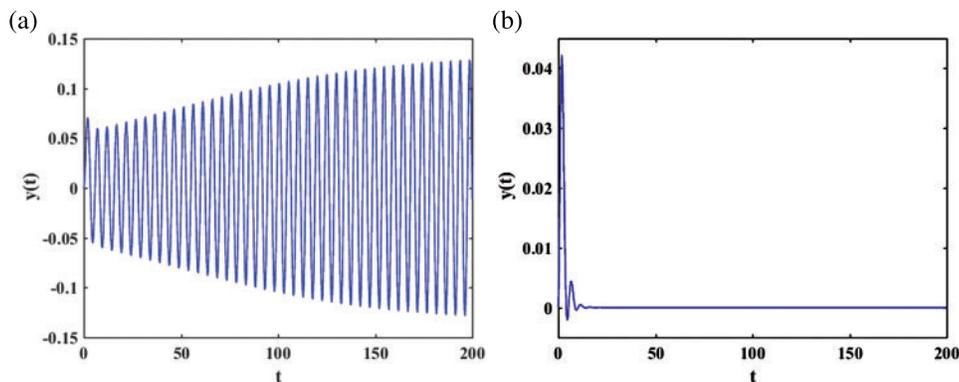
Figure 4: Time-domain response displacement of the galloping energy harvester: (a) $f = 1.225$; (b) $f = 0.625$

For the case of nontrivial solutions, since the displacement amplitude and voltage amplitude of the steady-state moments are proportional to each other, the response characteristics of the displacement

amplitude are similar to those of the voltage amplitude. Herein, only the response characteristics of the voltage amplitude are investigated.

Fig. 5 shows the variations of the response moments Ev and Ev^2 with tuning parameters σ. As the tuning parameter σ increases, Ev and Ev^2 will have two solutions in a certain range. Meanwhile, the multi-solution region enlarges with the increase of wind speed U. For example, for $U = 1$, the multi-solution region of Ev is [1.867, 2.373], and for $U = 1.6$, the multi-solution region of Ev is [1.996, 5.403]. The maximum Ev increases as the wind speed become larger, which is consistent with the results of Daqaq [24] and Xu et al. [25]. Ev^2 has similar results.
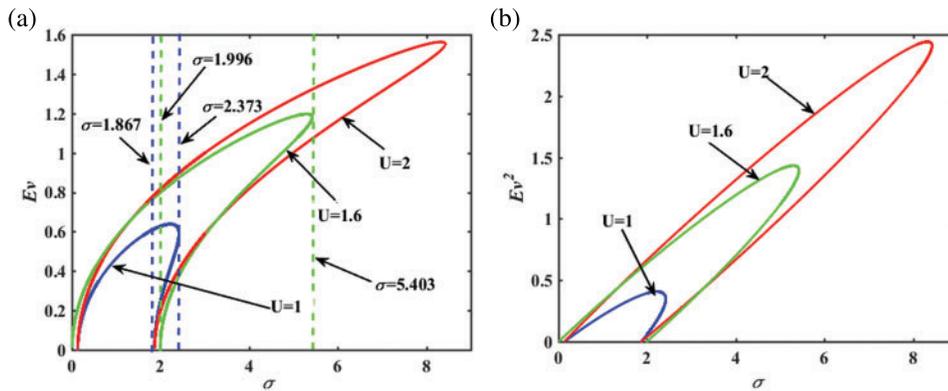
Figure 5: (a) First-order steady-state moment of voltage; (b) Second-order steady-state moment of voltage of the galloping energy harvester with tuning parameters

Fig. 6 shows the impact of the cubic stiffness coefficient k_2. On the response moments of voltage Ev and Ev^2. When $k_2 = 0$, the galloping energy harvester has only linear restoring force. The higher the wind speed, the greater Ev and Ev^2 will be. When $k_2 > 0$, Ev and Ev^2 always decreases with the increase of k_2, which means that the nonlinear restoring force hinders the voltage output. Meanwhile, the higher the wind speed is, the faster the falling speed of Ev and Ev^2. When k_2 exceeds a certain range (i.e., $k_2 > 1.5$), the wind speed has little effect on the voltage output. Therefore, the voltage output of the energy harvester can be controlled by adjusting the cubic coefficient k_2.
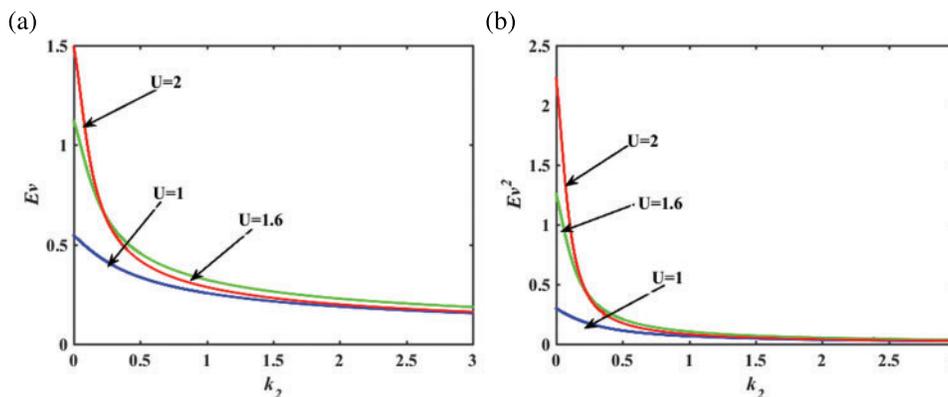
Figure 6: (a) First-order steady-state moment of voltage; (b) Second-order steady-state moment of voltage of the galloping energy harvester with the cubic stiffness coefficient k_2.

Fig. 7 shows the curve of the response moments Ev and Ev^2 vs. the excitation intensity F under different wind speed U. When the excitation intensity F is very small, no voltage is generated. When the excitation intensity F exceeds the critical value (i.e., $F > 0.05$ when $U = 1.6$), Ev and Ev^2 increases with the increase of the excitation intensity F. In particular, the greater the wind speed U is, the greater the critical value of excitation intensity F is, and the faster the Ev and Ev^2 increase. This means that the greater the wind speed, the more violent the impact of random factors on the galloping energy harvester, but more voltage can be obtained from the wind speed. Therefore, it is necessary to find a suitable value between wind speed and random interference.
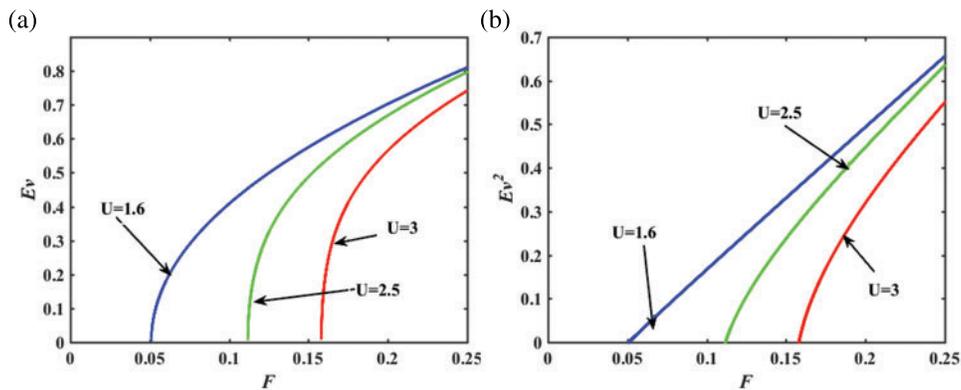
Figure 7: (a) First-order steady-state moment of voltage; (b) Second-order steady-state moment of voltage of the galloping energy harvester with the excitation intensity F.

Due to the fact that the spectral density of bounded noise is very complex, the analytical expression of PDF cannot be obtained by the currently known methods. Therefore, in order to further explore the impact of wind speed and random noise on the performance of the galloping energy harvester, Monte-Carlo simulation is used to numerically solve the stationary PDF of Eqs. (5) and (6). Fig. 8 shows the PDF of displacement and velocity under different wind speed. It can be seen that the PDF of displacement and velocity have similar curves in Figs. 8a and 8b, and both show two peaks and the "crater" phenomenon, which are caused by the galloping and demonstrates the quasi-periodic oscillatory properties of the galloping energy harvester.
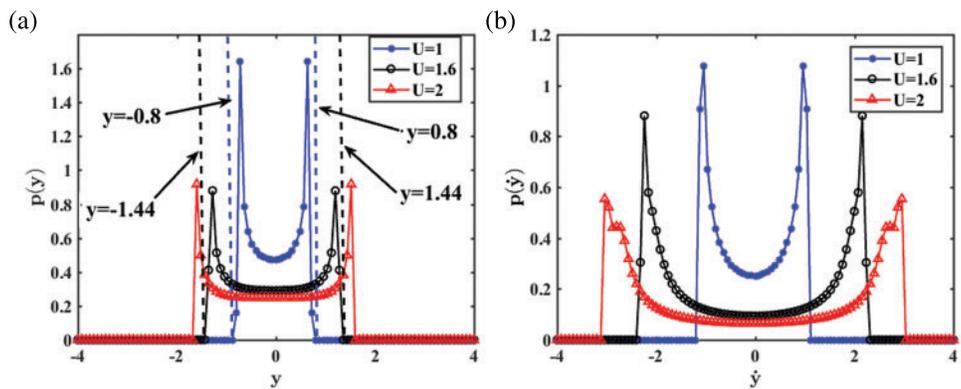
Figure 8: (a) The displacement PDF; (b) The velocity PDF of the galloping energy harvester with $\beta = 0.001$ and $f = 0.01$.

Meanwhile, the higher the wind speed U is, the stronger the periodic galloping vibration due to the enhanced aerodynamic instability, and the more prone the bluff body to vibration. For example, when $U = 1$, the vibration displacement is restrained into $[-0.8, 0.8]$. And when $U = 1.6$, the vibration displacement is restrained into $[-1.44, 1.44]$. It is worth noting that the amplitude of the bluff body cannot exceed the range of the galloping energy harvester. Therefore, the ambient wind speed should be further considered in practical application.

Fig. 9 shows the PDF of the displacement and velocity under different damping ratios ζ, respectively. All the curves have two peaks and the crater. As the different damping ratio ζ increases, the peak value of the displacement PDF decrease, and the range of vibration decreases. the velocity PDF has the opposite phenomenon. The reason is that increasing to damping ratios ζ increases the critical wind speed for galloping, which in turn weakens the performance of the galloping energy harvester. Therefore, when designing the galloping energy harvester, the damping ratios should be reduced as much as possible to improve the performance.
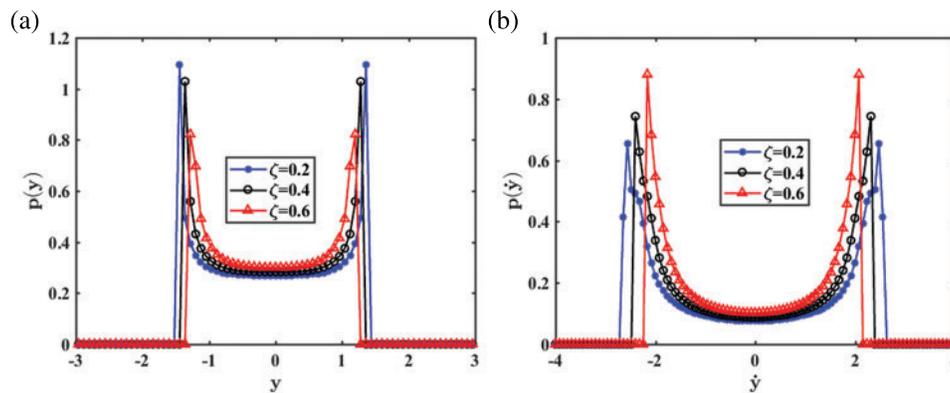
Figure 9: (a) The displacement PDF; (b) The velocity PDF of the galloping energy harvester with $\beta = 0.001, f = 0.01$ and $U = 1.6$ under the different damping ratios ζ.

Fig. 10 shows the PDF of the displacement and velocity under electromechanical coupling coefficients s. The curves in Figs. 10a and 10b are similar to Fig. 9a. The electromechanical coupling coefficient $s = \dfrac{\theta^2}{C_p M}$ includes the capacitance C_p and the bluff body mass M. In general, the bluff mass M is hardly variable, and the capacitance C_p depends on the piezoelectric (PZT) materials used. Therefore, Fig. 10 could provide theoretical guidance for the performance of the energy harvester with different PZT materials.
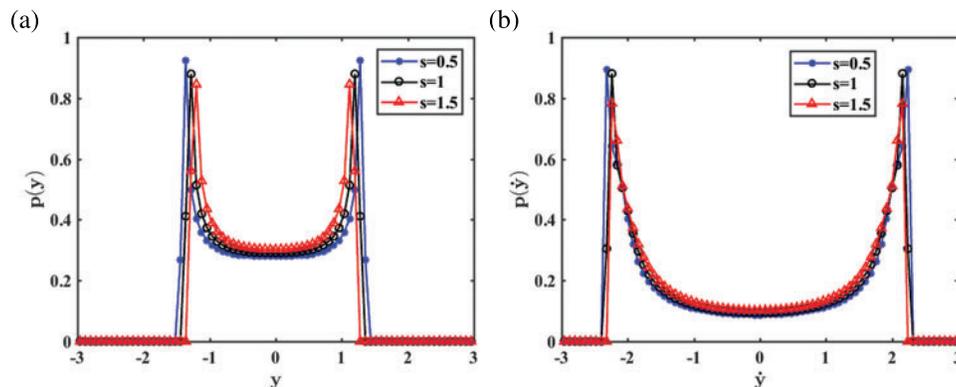
Figure 10: (a) The displacement PDF; (b) the velocity PDF of the galloping energy harvester with $\beta = 0.001, f = 0.01$ and $U = 1.6$ under the different electromechanical coupling coefficients s.

6 Conclusions

A galloping energy harvester under bounded parameter excitation is investigated theoretically. Due to the properties of the galloping phenomenon, the multi-scales method is employed to study the first-order approximate solution of the galloping energy harvester, and an expression for the solution is derived. Then the stability of the trivial solutions and nontrivial solutions are discussed, respectively. Analytical expressions for the LLE, which determines the stability of the trivial solution, are obtained. The numerical results show that the LLE reaches the maximum at the center of the unstable region, which is around the resonance region, and beyond the region is stability. The analytical expressions for the response moments of the nontrivial solutions are obtained by the moment method. The results show that the tuning parameters, the cubic stiffness coefficient, and the excitation strength, have a significant impact on the dynamic characteristics of the steady-state moments. The tuning parameters will cause the system to generate a multi-solution region. And the voltage output of the energy harvester can be controlled by adjusting the cubic coefficient. In addition, the stationary PDF was obtained by Monte-Carlo simulation. It found that the performance of the galloping energy harvester is correlated with wind speed, the damping ratio, and the PZT materials. The output voltage of the energy harvester can be increased by adjusting the damping rate and selecting suitable PZT materials. And the damping ratios should be reduced as much as possible when designing the galloping energy harvester. In conclusion, the stochastic response properties of the galloping energy harvester under bounded random parameter excitation are revealed. In the future, the relevant results can provide a guide for the optimization and design of energy harvesters.

Conflicts of Interest: The authors declare that they have no conflicts of interest to report regarding the present study.

References

1. Soni, P., Pal, A. K., Islam, S. H. (2019). An improved three-factor authentication scheme for patient monitoring using WSN in remote health-care system. *Computer Methods and Programs in Biomedicine, 182,* 105054.

2. Lanzolla, A., Spadavecchia, M. (2021). Wireless sensor networks for environmental monitoring. *Sensors, 21(4),* 1172.

3. Kim, D. S., Tran-Dang, H. (2019). Wireless sensor networks for industrial applications. In: *Industrial sensors and controls in communication networks*, Springer, Cham.

4. Miao, G., Fang, S., Wang, S., Zhou, S. (2022). A low-frequency rotational electromagnetic energy harvester using a magnetic plucking mechanism. *Applied Energy, 305,* 117838.

5. Yang, T., Cao, Q., Hao, Z. (2021). A novel nonlinear mechanical oscillator and its application in vibration isolation and energy harvesting. *Mechanical Systems and Signal Processing, 155,* 107636.

6. Huang, D., Han, J., Zhou, S., Han, Q., Yang, G. et al. (2022). Stochastic and deterministic responses of an asymmetric quad-stable energy harvester. *Mechanical Systems and Signal Processing, 168,* 108672.

7. Huang, D., Chen, J., Zhou, S., Fang, X., Li, W. (2021). Response regimes of nonlinear energy harvesters with a resistor-inductor resonant circuit by complexification-averaging method. *Science China Technological Sciences, 64(6),* 1212–1227.

8. Zhou, S., Zuo, L. (2018). Nonlinear dynamic analysis of asymmetric tristable energy harvesters for enhanced energy harvesting. *Communications in Nonlinear Science and Numerical Simulation, 61,* 271–284.

9. Yan, B., Zhou, S., Zhao, C., Wang, K., Wu, C. (2019). Electromagnetic energy harvester for vibration control of space rack: Modeling, optimization, and analysis. *Journal of Aerospace Engineering, 32(1),* 04018126.

10. Fang, S., Chen, K., Lai, Z., Zhou, S., Liao, W. H. (2023). Analysis and experiment of auxetic centrifugal softening impact energy harvesting from ultra-low-frequency rotational excitations. *Applied Energy, 331,* 120355.

11. Fang, S., Chen, K., Xing, J., Zhou, S., Liao, W. H. (2021). Tuned bistable nonlinear energy sink for simultaneously improved vibration suppression and energy harvesting. *International Journal of Mechanical Sciences, 212,* 106838.

12. Yang, K., Wang, J., Yurchenko, D. (2019). A double-beam piezo-magneto-elastic wind energy harvester for improving the galloping-based energy harvesting. *Applied Physics Letters, 115(19),* 193901.

13. Hu, G., Wang, J., Qiao, H., Zhao, L., Li, Z. et al. (2021). An experimental study of a two-degree-of-freedom galloping energy harvester. *International Journal of Energy Research, 45(2),* 3365–3374.

14. Bibo, A., Daqaq, M. F. (2014). On the optimal performance and universal design curves of galloping energy harvesters. *Applied Physics Letters, 104(2),* 023901.

15. Huang, D., Han, J., Li, W., Deng, H., Zhou, S. (2023). Responses, optimization and prediction of energy harvesters under galloping and base excitations. *Communications in Nonlinear Science and Numerical Simulation, 119,* 107086.

16. Tang, L., Zhao, L., Yang, Y., Lefeuvre, E. (2014). Equivalent circuit representation and analysis of galloping-based wind energy harvesting. *IEEE/ASME Transactions on Mechatronics, 20(2),* 834–844.

17. Sun, W., Seok, J. (2021). Novel galloping-based piezoelectric energy harvester adaptable to external wind velocity. *Mechanical Systems and Signal Processing, 152,* 107477.

18. Tan, T., Zuo, L., Yan, Z. (2021). Environment coupled piezoelectric galloping wind energy harvesting. *Sensors and Actuators A: Physical, 323,* 112641.

19. Zhou, S., Li, J., Wang, J., Li, G., Wang, Q. (2019). Vortex-induced vibrational tristable energy harvester: Design and experiments. *IOP Conference Series: Materials Science and Engineering, 531(1),* 012011.

20. Alhadidi, A. H., Daqaq, M. F. (2016). A broadband bi-stable flow energy harvester based on the wake-galloping phenomenon. *Applied Physics Letters, 109(3),* 033904.

21. McCarthy, J. M., Watkins, S., Deivasigamani, A., John, S. J. (2016). Fluttering energy harvesters in the wind: A review. *Journal of Sound and Vibration, 361,* 355–377.

22. Yang, K., Qiu, T., Wang, J., Tang, L. (2020). Magnet-induced monostable nonlinearity for improving the VIV-galloping-coupled wind energy harvesting using combined cross-sectioned bluff body. *Smart Materials and Structures, 29(7),* 07LT01.

23. Kitio Kwuimy, C. A., Litak, G., Borowiec, M., Nataraj, C. (2012). Performance of a piezoelectric energy harvester driven by air flow. *Applied Physics Letters, 100(2),* 024103.

24. Daqaq, M. F. (2015). Characterizing the response of galloping energy harvesters using actual wind statistics. *Journal of Sound and Vibration, 357,* 365–376.

25. Xu, M., Wang, B., Li, X., Zhou, S., Yurchenko, D. (2022). Dynamic response mechanism of the galloping energy harvester under fluctuating wind conditions. *Mechanical Systems and Signal Processing, 166,* 108410.

26. Yang, K., Abdelkefi, A., Li, X., Mao, Y., Dai, L. et al. (2021). Stochastic analysis of a galloping-random wind energy harvesting performance on a buoy platform. *Energy Conversion and Management, 238,* 114174.

27. Abdelkefi, A., Yan, Z., Hajj, M. R. (2013). Nonlinear dynamics of galloping-based piezoaeroelastic energy harvesters. *The European Physical Journal Special Topics, 222(7),* 1483–1501.

28. Yang, Y., Zhao, L., Tang, L. (2013). Comparative study of tip cross-sections for efficient galloping energy harvesting. *Applied Physics Letters, 102(6),* 064105.

29. Bibo, A., Alhadidi, A. H., Daqaq, M. F. (2015). Exploiting a nonlinear restoring force to improve the performance of flow energy harvesters. *Journal of Applied Physics, 117(4),* 045103.

30. Na, Y., Lee, M. S., Lee, J. W., Jeong, Y. H. (2020). Wind energy harvesting from a magnetically coupled piezoelectric bimorph cantilever array based on a dynamic magneto-piezo-elastic structure. *Applied Energy, 264,* 114710.

31. Wang, J., Geng, L., Zhou, S., Zhang, Z., Lai, Z. et al. (2020). Design, modeling and experiments of broadband tristable galloping piezoelectric energy harvester. *Acta Mechanica Sinica, 36(3),* 592–605.

32. Zhao, D., Hu, X., Tan, T., Yan, Z., Zhang, W. (2020). Piezoelectric galloping energy harvesting enhanced by topological equivalent aerodynamic design. *Energy Conversion and Management, 222,* 113260.

33. Sun, W., Guo, C., Cheng, G., He, S., Yang, Z. et al. (2022). Performance enhancement of galloping-based piezoelectric energy harvesting by exploiting 1:1 internal resonance of magnetically coupled oscillators. *Nonlinear Dynamics, 108(4),* 3347–3366.

34. Yang, T., Cao, Q. (2019). Dynamics and energy generation of a hybrid energy harvester under colored noise excitations. *Mechanical Systems and Signal Processing, 121,* 745–766.

35. Zhang, Y., Jiao, Z., Duan, X., Xu, Y. (2021). Stochastic dynamics of a piezoelectric energy harvester with fractional damping under Gaussian colored noise excitation. *Applied Mathematical Modelling, 97,* 268–280.

36. Yang, Z., Zhou, S., Zu, J., Inman, D. (2018). High-performance piezoelectric energy harvesters and their applications. *Joule, 2(4),* 642–697.

37. Safaei, M., Sodano, H. A., Anton, S. R. (2019). A review of energy harvesting using piezoelectric materials: State-of-the-art a decade later (2008–2018). *Smart Materials and Structures, 28(11),* 113001.

38. Zhao, L., Yang, Y. (2018). An impact-based broadband aeroelastic energy harvester for concurrent wind and base vibration energy harvesting. *Applied Energy, 212,* 233–243.

39. Sobhanirad, S., Afsharfard, A. (2019). Improving application of galloping-based energy harvesters in realistic condition. *Archive of Applied Mechanics, 89(2),* 313–328.

40. Wang, J., Sun, S., Hu, G., Yang, Y., Tang, L. et al. (2021). Exploring the potential benefits of using metasurface for galloping energy harvesting. *Energy Conversion and Management, 243,* 114414.

41. Hu, G., Wang, J., Tang, L. (2021). A comb-like beam based piezoelectric system for galloping energy harvesting. *Mechanical Systems and Signal Processing, 150,* 107301.

42. Zhao, L., Tang, L., Yang, Y. (2013). Comparison of modeling methods and parametric study for a piezoelectric wind energy harvester. *Smart Materials and Structures, 22(12),* 125003.

43. Ma, X., Zhou, S. (2022). A review of flow-induced vibration energy harvesters. *Energy Conversion and Management, 254,* 115223.

44. Huang, D., Zhou, S., Yang, Z. (2019). Resonance mechanism of nonlinear vibrational multistable energy harvesters under narrow-band stochastic parametric excitations. *Complexity, 2019,* 1050143.

45. Huang, D., Zhou, S., Li, R., Yurchenko, D. (2022). On the analysis of the tristable vibration isolation system with delayed feedback control under parametric excitation. *Mechanical Systems and Signal Processing, 164,* 108207.